Investigation of the Defect Distribution of Laser Contact Opening Applied to Poly-Si/SiNx Stacks

Bernd Steinhauser,* Varun Arya, Leonie Jakob, Friedemann D. Heinz, Christian Schmiga, Benjamin Grübel, Andreas A. Brand, Sven Kluska, and Jan F. Nekarda

Herein, an analysis on the impact of laser contact opening of TOPCon/SiNx stacks is presented. By etching in tetramethylammonium hydroxide (TMAH), the defect distribution in the interfacial tunnel oxide is accessed and analyzed. The defect density is significantly increased in areas where adjacent laser contact openings (LCO) overlap. Using microscopic photoluminescence (μ-PL) spectroscopy, it is verified that correlates with an increase in the local recombination rate and thus an increase in the $J_{0,Met}$. Therefore, overlapping LCO of SiNx in TOPCon/SiNx stacks should be avoided as much as possible. Furthermore, the investigations indicate that defects in the interfacial oxide are dominantly created along exposed structures like tips and edges of (etched-back) pyramids. A comparison of TOPCon/SiNx stacks with a variation of TOPCon thicknesses indicate that etch pits, and thus the defect density, related to LCO become more significant at lower thicknesses.

1. Introduction

Passivating contacts realized by a thin interfacial oxide and a heavily doped poly-Si layer (hereafter referred to as TOPCon) have demonstrated excellent surface passivation capabilities and cell efficiency potential.[1–5] The TOPCon technology is therefore considered for next generation solar cell concepts. The common industrial implementation—typically called i-TOPCon—features a boron emitter passivated by Al_2O_3/SiN_x at the front side on top of an n-type crystalline silicon base. The rear side is passivated by a TOPCon/SiNx stack. This concept already achieved excellent efficiencies of above 24%.[5–8] While both sides are typically contacted by screen printing and

B. Steinhauser, V. Arya, L. Jakob, F. D. Heinz, C. Schmiga, B. Grübel,
A. A. Brand, S. Kluska, J. F. Nekarda
Division Photovoltaics
Fraunhofer-Institute for Solar Energy Systems
Heidenhofstr. 2, 79110 Freiburg, Germany
E-mail: bernd.steinhauser@ise.fraunhofer.de

subsequent fast-firing, other methods to create the metal contacts are considered as well: as a viable alternative Grübel et al. successfully demonstrated, bifacial laser contact opening (LCO) and subsequent plating of nickel, copper, and silver.[9] A sketch of this cell concept is shown in **Figure 1** (left). Copper-plated contacts allow for a significant reduction of silver consumption resulting in an overall lower cost of ownership.[10,11] However, damage to the TOPCon layer due to LCO can be a critical factor. Haase et al. and Arya et al. demonstrated that the severity of this laser damage is dependent on the thickness of the poly-Si layer.[3,12] In case of LCO on a phosphorus emitter, it is known that a main source for increased recombination is due to amorphization of parts of the region treated by the laser.[13] The laser-induced amorphization and defects can be thermally annealed such that the additional recombination due to the laser treatment that can be minimized.[14–16] For laser processing of poly-Si, it is known that such amorphization can take place as well.[17] However, for poly-Si surface passivation, the interfacial oxide (SiO_x) plays a crucial role and pinholes can result in increased recombination rates.[18,19] While amorphization is reversible, damage to the SiO_x by laser process could therefore lead to permanently reduced surface passivation performance. Damage to the SiO_x could result in an irreversible increase of the contact recombination due to the laser process. Therefore, the state and integrity of the SiO_x after LCO are of high interest. This can be investigated by defect etching in tetramethylammonium hydroxide (TMAH), an etch that has a high etch rate for silicon, but a very low etch rate for SiO_x.[20] It can be used to create local etch pits that magnify and highlight defects in the silicon oxide, as was demonstrated for poly-Si/SiO_x/c-Si interfaces by Wietler et al.[21] Here, the high selectivity in the etching behavior is important to pin down the defects in the SiO_x and prevent excessive widening of the point defects or even creating new ones due to etching.
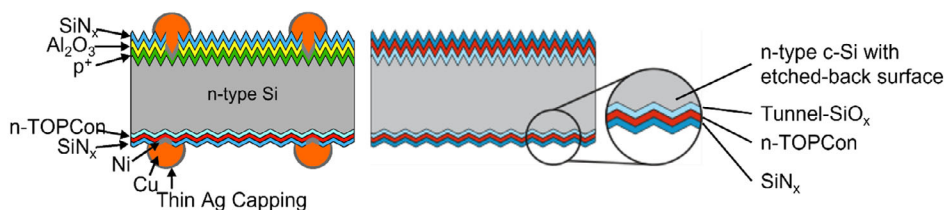
2. Results and Discussion

The main objective of this investigation is to acquire more information about the recombination properties of LCO on poly-Si/

Figure 1. Left: schematic of the target cell design. Right: schematic of the investigated simplified sample design. Both sides are passivated by TOPCon/SiN$_x$ stacks. The bulk material is n-type, no emitter diffusion took place. Both sides were textured, but on one side, the texture was etched-back as done for solar cells to remove the emitter on the rear side.
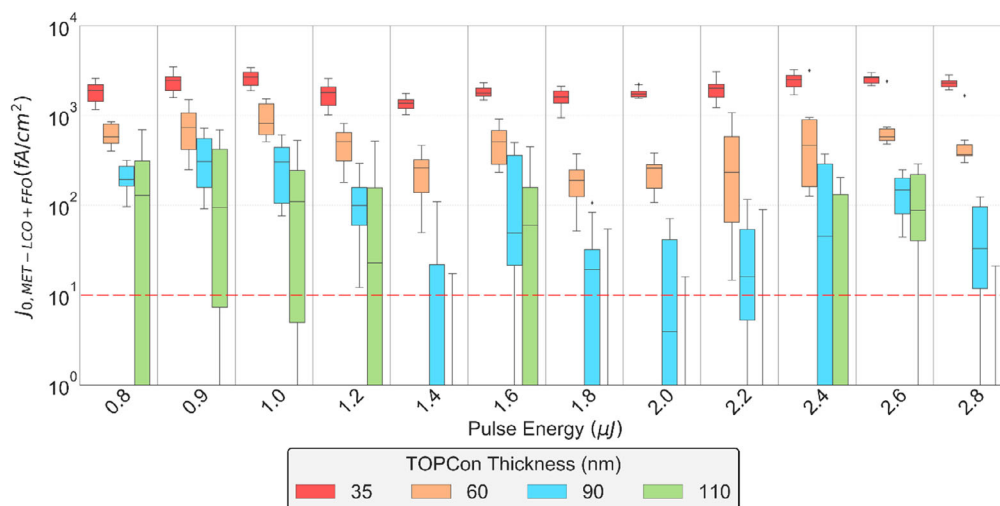

Figure 2. $J_{0,Met}$ in the laser processed area after laser contact opening (LCO) and fast-firing oven (FFO) for a variation in the TOPCon thickness as well as the laser pulse energy. The $J_{0,Met}$ corresponds to the local increase in the recombination *on top* of $J_{0,Bulk}$ and $J_{0,Pass}$ determined from passivated reference fields and being subtracted in the evaluation. Therefore, $J_{0,Met} = 0$ would appear exactly like a passivated surface since the laser processing in this case resulted in no change in the recombination. Even for low, nonzero $J_{0,Met}$ the uncertainty in the evaluation is high. Therefore, values below the dashed red line (10 fA cm^{-2}) should be treated with caution. The graph was taken from Arya et al.,[12] some minor adjustments were made. Reproduced under the creative commons license CC-BY 4.0.[24]

SiN$_x$ stacks. The samples used for this investigation were already studied by Arya et al.[12] The basic structure of these samples is shown in Figure 1 (right). The rear-side surface was textured with random pyramids, but the texture is etched-back as done commonly in the fabrication of industrial silicon solar cells. Both sides of the samples are passivated by TOPCon/SiN$_x$ stacks. **Figure 2** shows the recombination $J_{0,Met}$ after LCO and thermal treatment in a fast-firing oven (FFO) as determined by Arya et al.[12] The $J_{0,Pass}$ of the passivated surface was $\approx$7 fA cm^{-2}. For an in-depth discussion of the general trends, please refer to the cited paper.[12] In the figure, $J_{0,Met}$ is shown for a variation of the poly-Si thickness from 35 to 110 nm as well as the laser pulse energy from 0.8 up to 2.8 µJ. It should be noted that the plotted value accounts only for additional J_0 recombination on top of $J_{0,Pass}$ of the passivated surface and $J_{0,Bulk}$ of the bulk. A value of $J_{0,Met} = 0$ would mean that the laser had no additional impact on the recombination and a laser-processed area would exhibit the same recombination as a non-treated, passivated surface. For 60, 90, and 110 nm poly-Si, it can be observed that for laser pulse energies in the range of $\approx$1.4–2.2 µJ, the determined $J_{0,Met}$ is generally lower compared to laser pulse energies outside this range. For 35 nm poly-Si, the $J_{0,Met}$ is generally high

and no clear trend was observed. For lower pulse energies, an increase in $J_{0,Met}$ was observed. Arya et al. concluded that this was caused by the pulse-to-pulse overlap being too high for the spot size. An indication for this is that in Figure S1, Supporting Information, for a laser energy of 1.2 µJ, the size and position of the single laser pulses cannot be estimated. The excessive overlap would be the result of overadjustment, due to the necessity of adjusting the pulse-to-pulse distance for each laser pulse energy separately, as the opening size changes with the laser energy. Such overlap is necessary for LCO to form a line that results in a nearly homogeneous finger width after subsequent plating. If the pulse-to-pulse distance is increased too much, a significant limitation in the finger conductivity could be the result. If LCO is combined with other metallization techniques like screen printing or evaporation, it might be possible to avoid overlap completely. For the very high laser pulse energies, the increase in $J_{0,Met}$ is explained by the increased damage to the poly-Si layer. In the following, we investigate the plausibility of these theses.

First, the TMAH etch is applied to reference samples. **Figure 3** (left) therefore shows the etch pit distribution on a sample that was not treated by LCO. Here, the SiN$_x$ layer was removed
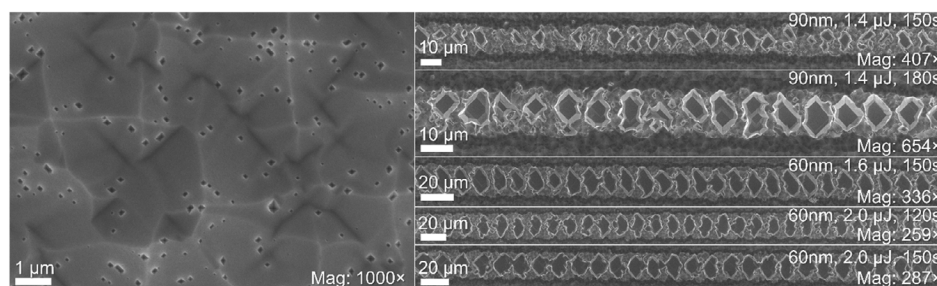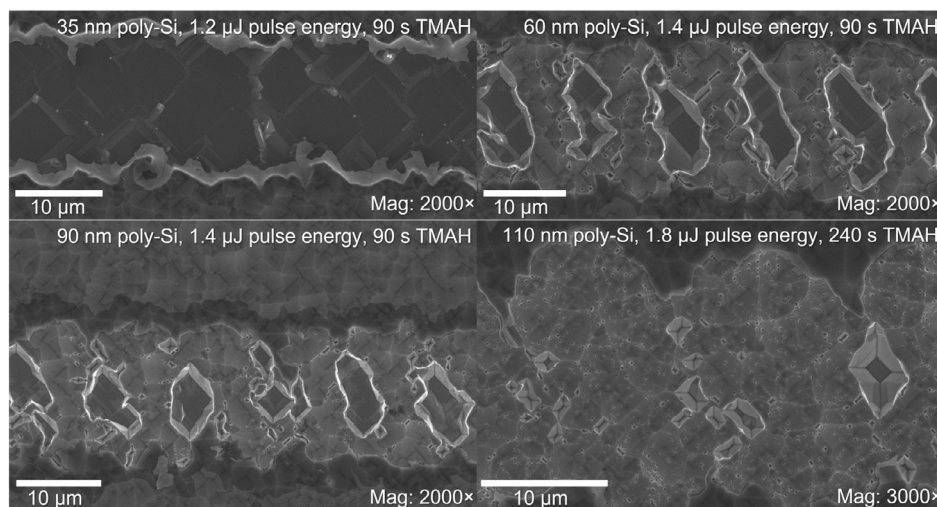
Figure 3. Left: etch pit distribution determined by scanning electron microscope (SEM) on a reference sample without laser processing. Right: collage of various lines investigated after the tetramethylammonium hydroxide (TMAH) etch using a SEM. The additional information gives the thickness of the TOPCon layer, the used laser energy, and the TMAH etching time.

wet-chemically before applying the TMAH etch for 240 s. A significant amount of etch pits was determined on the sample randomly distributed over the investigated area. Figure 3 (right) shows a series of low-magnification overview images for a selection of samples including the used poly-Si thickness, laser pulse energy, and TMAH etch time. For all five shown samples, large etch pits were observed. These etch pits are periodically distributed along the LCO line. For the upper two cases, the etch pit distribution shows stronger variation in size, shape, as well as positioning. For the lower three cases, the etch pits are very comparable in size and shape. The first investigation in Figure 3 (left) was important, since it indicates what kind of etch pit distribution—and therefore defect distribution in the oxide—would be expected for the used combination of sample surface, tunnel oxide, TOPCon layer, and postdeposition anneal. Since the defect distribution in this case seems to be random, etch pit patterns can—with high certainty—be attributed to the laser processing. The investigations in Figure 3 (right) were important, since discussing local effects at high resolution are only meaningful if the conclusions of the investigation can be applied to the majority of laser pulses at this poly-Si thickness and laser

pulse energy. While—as shown in the upper two lines—some inhomogeneities were observed, the structures for most lines were found to be very regular indicating a high reproducibility of the laser treatment for subsequent pulses.

With the usefulness of the method being verified, the next investigation focuses on the differences in the defect distribution for the various poly-Si thicknesses. **Figure 4** shows the created etch pits for each poly-Si thickness. For 35 nm poly-Si, the LCO line is clearly visible, but almost no structure was found within the width of the line after etching. For 60 and 90 nm, large etch pits were found periodically. Smaller etch pits can be spotted in between the large etch pits. For the largest poly-Si thickness of 110 nm, no comparable structures were observed, even though the etch time was much longer than for the smaller poly-Si thicknesses. Instead, many small etch pits as well as some medium-sized etch pits can be observed in the scanning electron microscope (SEM) image.

Especially, this last image of the 110 nm sample clarifies the formation of the large etch pits, since an accumulation of medium-sized etch pits can be observed in the connecting area of pulses. Thus, in areas where the defect density in the oxide is

Figure 4. Etch pit distribution determined by SEM for a variation in the poly-Si thickness from 35 to 110 nm poly-Si. For 35 and 110 nm, there were no SEM images available for 1.4 µJ pulse energy and 90 s TMAH etch time. Thus, images for a different parameter set are shown for comparison. The magnification for the 110 nm sample is higher by a factor of 1.5. It is mainly for this reason that the laser spot size appears to be much larger and not due to the higher pulse energy.

high, the small etch pits grow enough to connect to neighboring etch pits, lifting off the oxide in between. They then merge into medium-sized etch pits and finally, if the defect density is high and the etching time is long enough, large etch pits. This is further supported by a comparison of samples featuring the same poly-Si thickness and laser pulse energy but a variation in the etch time from 90 to 240 s. This variation is not shown but was performed to verify the thesis. This effect also helps to understand the result observed for 35 nm poly-Si. In this case, the defect distribution must have been so high that the oxide was removed completely even for the shortest etching time. The result is a very large "etch pit" that spans the whole line. These observations are in-line with the results for $J_{0,Met}$, which was found to be much larger for 35 nm poly-Si compared to the higher thicknesses (see Figure 2). Furthermore, the high defect distribution is not surprising as 35 nm poly-Si thickness is significantly later the damage-free threshold of ≈60 nm on planar surface according to Haase et al.,[3] especially considering that the surface of our samples was rougher than a planar surface. In contrast, the defect distribution in the tunnel oxide must be much lower for 110 nm poly-Si since despite the slightly higher laser pulse energy and significantly higher etching time no large etch pits were formed. Instead—apart from a couple of medium-sized etch pits—the distribution seems more comparable to the reference sample in Figure 2 (left). This matches the determined $J_{0,Met}$ for this thickness and laser pulse energy, meaning that the increase in recombination due to the laser processing is very low.

As mentioned earlier, large etch pits can be observed periodically in Figure 4 for 60 and 90 nm poly-Si. This was further analyzed for a sample with 60 nm poly-Si and a variation of the laser pulse energy, as shown in **Figure 5**. The figure shows the etch pit distribution for six laser pulse energies ranging from 1.2 to 2.2 μJ. The lowest pulse energy of 1.2 μJ is close to the ablation threshold of ≈0.9 μJ on these structures. In our experiments, 1.2 μJ was the lowest pulse energy for which the contact opening was of sufficient size. In addition, orange ellipses were added to each image indicating the approximate position and shape of

LCO pulses. Due to the Gaussian distribution of the pulse energy, pulse position and boundary are not absolute but extend to some degree beyond orange lines. For the lowest laser pulse energy of 1.2 μJ, almost the whole line is covered by large etch pits that do not seem to be regularly distributed. The position of the laser pulses could not be determined. For 1.4–1.8 μJ, regularly distributed large etch pits were observed. The positions of the large etch pits correlate with the approximate region in which the laser pulses overlap. For the laser pulse energy of 1.6 μJ in between, large etch pits were observed but not as regularly distributed and the laser pulse position could not be approximated. For the higher laser pulse energies of 2.0 and 2.2 μJ, again large etch pits were observed, but in this case, they extend toward the middle of the laser spots.

The images shown for 1.4 and 1.8 μJ in Figure 5 clearly hint that the large etch pits form mainly in the overlap region of pulses. Due to the overlap of the laser pulses, these regions receive multiple laser treatments. While there is no direct pulse-to-pulse interacting—meaning that the time between the pulses is significantly higher than the cool-down time—this still seems to affect the tunnel oxide significantly resulting in a higher etch pit density and therefore a higher defect density. While usually—due to the Gaussian distribution of the laser energy—the highest defect density would be expected in the middle of the laser spot, the impact of the multiple treatment is larger for medium laser pulse energies. As shown in Figure 5 for pulse energies of 1.2 and 1.6 μJ, this could not be observed for these cases. This is likely due to the overlap being chosen too high. For this reason, the position of the laser spots cannot be clearly defined and the etch pits due to pulse overlap cover most of the line.

At the higher pulse energy of 2.0 and 2.2 μJ, the large etch pits extend toward the middle of the laser spot. This indicates that at these high pulse energies, the pulse energy in the middle is large enough to create a high defect density, which is in accordance with the increase in $J_{0,Met}$ that was observed in Figure 2.

The investigations in Figure 5 indicate that the defect density in the overlap regions is significantly increased. However, it
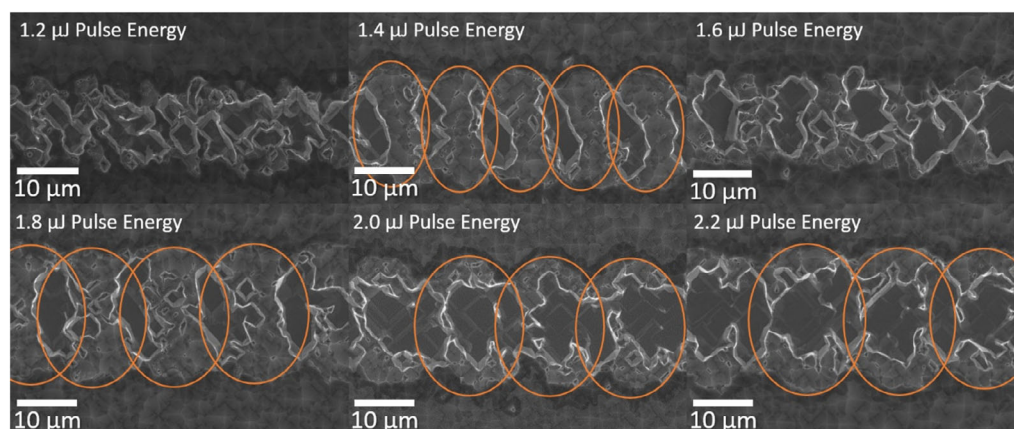
Figure 5. Etch pit distribution determined by SEM for a variation in the laser pulse energy. The poly-Si thickness for these samples was 60 nm, the TMAH etch time was 90 s. The approximate laser pulse position and size is indicated by orange ellipses. In case of 1.2 and 1.6 μJ, the laser pulse positions remain unclear. The magnification for all images was 2000×. For reference, Figure S1, Supporting Information, shows corresponding images acquired by optical microscopy directly after LCO.
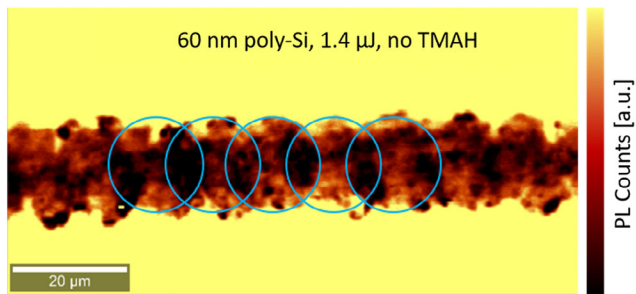
Figure 6. Scan of the photoluminescence signal acquired by microscopic photoluminescence (μ-PL). The blue ellipses indicate the approximate position of the laser pulses. The sample featured 60 nm poly-Si and was treated with a laser pulse energy of 1.4 μJ. No TMAH etch was performed on this sample meaning that the recombination state after LCO and FFO is captured.

could be possible that the impact on the recombination is insignificant. To investigate this, **Figure 6** shows the scan performed by microscopic photoluminescence (μ-PL) for 60 nm poly-Si and 1.4 μJ laser pulse energy. The sample was not treated with TMAH meaning that the scan shows the remaining integrity of the surface passivation after laser processing and firing. Again, the approximate positions of the laser pulses are indicated as blue ellipses. The color bar scale indicates the PL intensity correlating to the local recombination rate, that is, a black area indicates very high and yellow very low recombination rate. With the used combination of laser processing and poly-Si thickness, the line is clearly visible indicating the significant impact of laser processing, which is in accordance with the high $J_{0,\mathrm{Met}}$ in the range of 200–300 fA cm^{-2} observed for this combination (see Figure 2). While not as clearly visible as the etch pit distribution in Figure 5, it can be observed that in the overlap region the recombination rate is significantly increased. It is therefore expected that the localized $J_{0,\mathrm{Met}}$ within this area is increased as well. This means that the increased defect density in the overlap area has significant impact on the recombination and therefore pulse overlap should be avoided as much as possible. It should be noted that a modification in the surface morphology by the laser could also lead to a variation in the observed PL signal. However, according to images by optical microscopy, the area in the overlap

region indicates lower surface roughness than in the mid-pulse area (where the laser energy is the highest). Thus, the morphology seems more comparable to the passivated surface not modified by the laser.

One additional conclusion that can be drawn from the results is that placing multiple laser pulses at the same spot is expected to have negative consequences. Such an approach of consecutive laser pulses was investigated by Brand[15,16] for LCO of SiN$_x$ on phosphorous emitters and found to reduce the laser damage. However, in case of poly-Si—based on our findings—an advantage due to consecutive laser pulses is not expected.

Apart from the impact of pulse overlap another observation can be made when investigating these samples. **Figure 7** shows large-magnification images of two samples. Here, the poly-Si thickness and laser pulse energy are of minor interest. Instead, the images indicate that etch pits are—at these low TMAH etching times—formed dominantly at tips or edges of the (partially) removed pyramids of the former texture. This can be explained by self-interaction of the laser pulses at these exposed structures resulting in a local increase in the induced energy.[22] Due to this local increase in the energy, it is expected that the threshold for damage-free LCO on such etched-back surfaces is increased compared to an actual planar surface. This is in accordance with the findings in Figures 2 and 4 where the impact of LCO for 60 nm and even 90 nm is higher than 110 nm, meaning that the penetration depth of the laser pulse is more than 60 nm and thus higher than the threshold estimated by Haase et al. for planar surfaces.[3] In addition, it should be considered that differences in the sample processing like the deposition technique and process for the capping layer (SiN$_x$) and the used laser system could influence the threshold as well.

3. Conclusion

Lifetime samples passivated by TOPCon/SiN$_x$ stacks were analyzed after laser contact opening. TMAH etching was used to analyze the defect distribution and density in the interfacial tunnel oxide. It was found that the defect density is significantly increased in areas where neighboring laser pulses overlap. This increased defect density leads to an increase in the local recombination rate and thus an increase in the $J_{0,\mathrm{Met}}$.
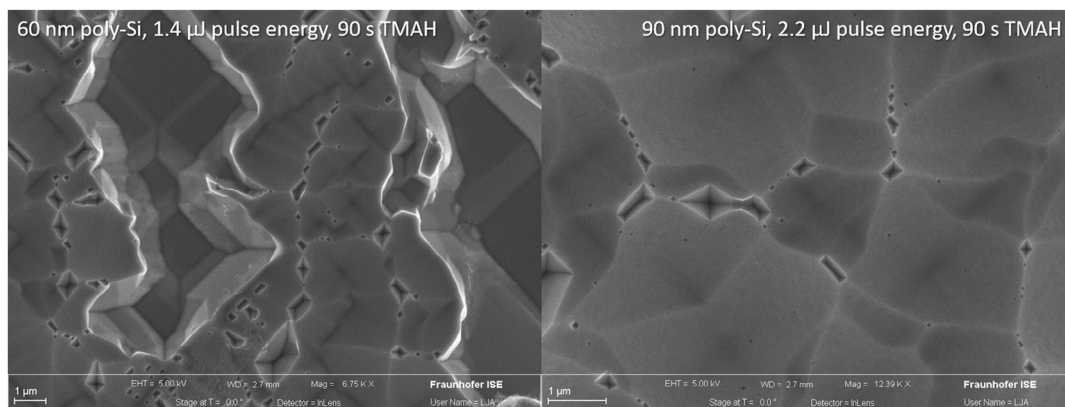
Figure 7. Etch pit distribution determined by SEM indicating that etch pits form often at tips or edges of the etched-back pyramids.

Therefore, laser pulse overlap should be avoided as much as possible for laser ablation of SiN_x in TOPCon/SiN_x stacks. Furthermore, the investigations indicated that defects in the interfacial oxide are dominantly created along exposed structures like tips and edges of (etched-back) pyramids. This was attributed to the self-interaction of the laser pulses. Furthermore, the comparison of different TOPCon thicknesses indicated that etch pits, and thus the SiO_x defects, related to LCO become more significant for lower thicknesses. This influence of the TOPCon thickness could also mean that there is a lower limitation on the usable TOPCon thickness for LCO/plating.

4. Experimental Section

Czochralski-grown silicon wafers of M2 size (156.75 mm length and 210 mm diameter) with a base resistivity of $1\,\Omega\,cm$ were used. Detailed results of these wafers, for example, on the recombination and contacting properties, were reported and discussed by Arya et al.[12]

After saw damage removal, the wafers were textured in KOH. The texture on one side (hereafter referred to as "rear side") was then removed in a solution of HNO_3 and HF to create a rear surface comparable to industrial tunnel oxide passivated contact (i-TOPCon) solar cells (after the etch-back of the emitter diffusion on the rear side). After cleaning the wafers in SC1 (8% NH_4OH with added H_2O_2), SC2 (8% HCl with added H_2O_2) and HNO_3, each followed by a dip in HF, a thin tunnel oxide layer was thermally grown in a tube furnace. Both sides were then coated by direct-plasma plasma-enhanced chemical vapor deposition (PECVD) of the TOPCon layer followed by a nitrogen anneal at $900\,^\circ C$ for crystallization. On the rear side, the TOPCon layer thickness was varied from 35 to 110 nm. SiN_x with $n = 2.03$ and a thickness of 70 nm was deposited on both sides as an optical layer as well as a hydrogen source. For the deposition of SiN_x, a MeyerBurger MAiA in-line PECVD tool was used featuring a microwave, quasi-remote plasma source. The SiN_x was then removed again by LCO using an UV ultrashort-pulse laser (355 nm wavelength, 200 kHz repetition rate, less than 15 ps pulse duration) on the rear side in a chessboard-like layout featuring a wide variation in the used laser energy (see Arya et al.[12] for details). The spot size was 24 µm, the scanning speed was adjusted between 0.6 and $3.5\,m\,s^{-1}$ depending on the pulse energy and thus the size of the opening in the SiN_x. To reverse some of the damage due to the laser processing as well as hydrogenation of the TOPCon layer, the samples were fired in a fast-firing furnace at an actual wafer temperature of approx. $720\,^\circ C$. The wafer temperature profile during firing was determined on a reference sample of the same design using a type-K thermocouple.

For the investigations of the defect distribution single laser fields were cut out of the chessboard-like structure using a laser cutting process creating samples of $\approx 2 \times 2\,cm^2$ size, each featuring LCO lines processed with a single laser pulse energy. These samples were then first dipped in 1% HF to remove any exposed oxide and subsequently etched in 15% TMAH at $80\,^\circ C$. The TMAH-etching time was varied from 60 to 210 s. The samples were then investigated using a SEM to gather information about the created etch pit structures. The acceleration voltage in the SEM was kept constant at 5 kV. For the reference sample that was not processed by the laser, the SiN_x was first removed in buffered HF and then the sample was etched in TMAH with an etching time of 210 s. To examine the lateral differences in the recombination rates, a sample was scanned by microscopic µ-PL. This sample was processed as outlined earlier but without etching the poly-Si and SiN_x, meaning that the poly-Si is still in place and the recombination state after LCO and FFO is captured. A detailed description of the experimental µPL setup was given by Heinz et al.[23] For the measurements shown here, an excitation wavelength of 785 nm with a power of 40 mW on the sample surface was used. The laser light was focused using a $50\times$, $N_A = 0.65$ lens. The step size of the map was 250 nm and the integration time per pixel was 0.5 s.

Supporting Information

Supporting Information is available from the Wiley Online Library or from the author.

Conflict of Interest

The authors declare no conflict of interest.

Data Availability Statement

Research data are not shared.

[1] F. Feldmann, M. Bivour, C. Reichel, M. Hermle, S. W. Glunz, *Sol. Energy Mater. Sol. Cells* **2014**, *120*, 270.

[2] U. Römer, R. Peibst, T. Ohrdes, B. Lim, J. Krügener, E. Bugiel, T. Wietler, R. Brendel, *Sol. Energy Mater. Sol. Cells* **2014**, *131*, 85.

[3] F. Haase, C. Hollemann, S. Schäfer, A. Merkle, M. Rienäcker, J. Krügener, R. Brendel, R. Peibst, *Sol. Energy Mater. Sol. Cells* **2018**, *186*, 184.

[4] A. Richter, R. Müller, J. Benick, F. Feldmann, B. Steinhauser, C. Reichel, A. Fell, M. Bivour, M. Hermle, S. W. Glunz, *Nat. Energy* **2021**, *6*, 429.

[5] D. Chen, Y. Chen, Z. Wang, J. Gong, C. Liu, Y. Zou, Y. He, Y. Wang, L. Yuan, W. Lin, R. Xia, L. Yin, X. Zhang, G. Xu, Y. Yang, H. Shen, Z. Feng, P. P. Altermatt, P. J. Verlinden, *Sol. Energy Mater. Sol. Cells* **2020**, *206*, 110258.

[6] M. Osborne, *PV Tech.* **2020**, *14*, 12.

[7] F. Fertig, in *IEEE Journal of Photovoltaics,* September **2021**, *12*, 22.

[8] J. Bao, C. Chen, Z. Qiao, Z. Du, Z. Liu, J. Chen, *Photovolt. Int.* **2021**, 64.

[9] B. Grübel, G. Cimiotti, V. Arya, T. Fellmeth, F. Feldmann, B. Steinhauser, S. Kluska, T. Kluge, D. Landgraf, M. Glatthaar, in *36th EU PVSEC*, WIP GmbH & Co Planungs-KG in Munich, Germany, **2019**, pp. 167–171.

[10] B. Steinhauser, B. Grübel, S. Nold, V. Arya, C. Schmiga, S. Kluska, A. A. Brand, F. Feldmann, N. Bay, X. Gay, M. Passig, M. Glatthaar, in *37th EU PVSEC*, WIP GmbH & Co Planungs-KG in Munich, Germany, **2020**, pp. 179–183.

[11] S. Kluska, T. Hatt, B. Grübel, G. Cimiotti, C. Schmiga, V. Arya, B. Steinhauser, F. Feldmann, J. Bartsch, B. S. Goraya, S. Nold, A. A. Brand, J. F. Nekarda, M. Glatthaar, S. W. Glunz, *Photovolat. Int.* **2020**, *44*, 98.

[12] V. Arya, B. Steinhauser, B. Gruebel, C. Schmiga, N. Bay, D. Brunner, M. Passig, A. A. Brand, S. Kluska, J. Nekarda, *Phys Status Solidi A* **2020**, *217*, 2000474.

[13] F. Meyer, A. Büchler, A. A. Brand, M. K. Dasa, J. F. Nekarda, R. Preu, *Appl. Phys. A* **2018**, *124*, 237.

[14] N. Bay, A. A. Brand, A. Büchler, J. Burschik, S. Kluska, H. H. Kuehnlein, M. Passig, D. Pysch, M. Sieber, *Energy Proc.* **2017**, *124,* 823.

[15] A. A. Brand, A. Knorz, R. Zeidler, J.-F. Nekarda, R. Preu, E. W. Reutzel, in *Laser Material Processing for Solar Energy* Society of Photo-Optical Instrumentation Engineers in Bellingham, Washington, USA, **2012**, p. 84730.

[16] A. A. Brand, F. Meyer, J. F. Nekarda, R. Preu, *Appl. Phys. A* **2014**, *117*, 237.

[17] S. Schäfer, A. Mercker, A. Köhler, T. Neubert, L. Mettner, B. Wolpensinger, V. Mertens, R. Peibst, *J. Appl. Phys.* **2021**, *129*, 133103.

[18] J.-I. Polzin, S. Lange, S. Richter, A. Moldovan, M. Bivour, C. Hagendorf, M. Hermle, S. W. Glunz, F. Feldmann, *Sol. Energy Mater. Sol. Cells* **2020**, *218*, 110713.

[19] F. Feldmann, G. Nogay, J.-I. Polzin, B. Steinhauser, A. Richter, A. Fell, C. Schmiga, M. Hermle, S. W. Glunz, *IEEE J. Photovolt.* **2018**, *8*, 1503.

[20] O. Tabata, R. Asahi, H. Funabashi, K. Shimaoka, S. Sugiyama, *Sens. Actuators A: Phys.* **1992**, *34*, 51.

[21] T. F. Wietler, D. Tetzlaff, J. Krügener, M. Rienäcker, F. Haase, Y. Larionova, R. Brendel, R. Peibst, *Appl. Phys. Lett.* **2017**, *110*, 253902.

[22] A. Knorz, M. Peters, A. Grohe, C. Harmel, R. Preu, *Prog. Photovolt: Res. Appl.* **2009**, *17*, 127.

[23] F. D. Heinz, L. E. Mundt, W. Warta, M. C. Schubert, *Phys. Status Solidi RRL* **2015**, *9*, 697.

[24] Creative Commons, License CC-BY 4.0, https://creativecommons.org/licenses/by/4.0/, (accessed: August 2021).